Lipid nanotubes as an organic template for the fabrication of carbon nanostructures by pyrolysis

Kristina Jajcevic[1], Ashlin Mario Sequeira[1], Jana Kalbacova[2,3], Dietrich R.T. Zahn[3], Kaori Sugihara[4, 1]✉

[1]Department of Physical Chemistry, University of Geneva, Quai Ernest Ansermet 30, 1211 Geneva 4, Switzerland

[2]HORIBA Jobin Yvon GmbH, D-64625 Bensheim; Neuhofstr. 9, Germany

[3]Semiconductor Physics, Chemnitz University of Technology, D-09107 Chemnitz, Germany

[4]Institute of Industrial Science, The University of Tokyo, 4-6-1 Komaba Meguro-Ku, Tokyo 153-8505, Japan

✉email: kaori-s@iis.u-tokyo.ac.jp

ABSTRACT:

We demonstrate the fabrication of carbon nanoribbons with a width of 40 nm based on fixation and pyrolysis of an organic template, lipid nanotubes. To our best knowledge, this is the smallest feature size achieved by pyrolysis of surface-patterned organic templates. Such a pyrolytic carbon nanostructure can be used for electronics and sensing applications in future.

Carbon nano- to microstructures made of PDMS[1] or SU8[2-11] patterns fabricated by lithography followed by pyrolysis have found wide applications[12-17] in carbon-microelectromechanical systems (Carbon-MEMS),[3] biosensing,[18-20] electronics such as capacitors,[21] and as a method to modify cantilevers for atomic force microscopy.[22] Their structures are typically between pyrolytic carbon, where defects in graphite interconnect graphene sheets, and glassy carbon, which is a disordered carbon allotrope primarily consisting of non-graphitic sp^2-bonds. They exhibit excellent chemical resistance, thermal stability, biocompatibility, and can present semiconductor-

type electrical properties. Additives in the photoresist such as metal[23,24] or silicon[25] form organic-inorganic hybrid structures upon pyrolysis, whereas combining polymers after pyrolysis produces polymer-carbon composites for electrodes.[26] Since its first demonstration by the Whitesides group in the late 90s, the method has been improved towards better controllability, the formation of 3D structures, and smaller feature sizes by optimization of the fabrication parameters or by an introduction of advanced lithography methods such as two-photon lithography.[11] To date, most of the surface-patterned carbon structures fabricated by these approaches has a structure size at micro- to submicrometer scale. Etching the carbon structure afterwards can further reduce the structure size below 100 nm, yet this requires an extreme optimization.[27] To go beyond 100 nm and to potentially create 3D structures that are difficult to be achieved by conventional lithography, nature-made nanostructures,[28-30] biomolecules, can be a cheap and safe alternative scaffold for pyrolysis. Towards this direction, Nakano and coworkers created fluorescent carbon nanowires by pyrolysis of DNA fibers.[31]

In this work, we demonstrate the fabrication of carbon nanoribbons by pyrolysis of lipid nanotubes (LNT) that have a width of 40 nm. To our best knowledge, this is the smallest feature size achieved by pyrolysis of organic templates patterned on substrates. LNTs used in this work have been previously discovered and extensively characterized in our group.[32-36] They are single-wall lipid tubes with an outer diameter of 19.1 ± 4.5 nm, self-assembled with the main lipid of bacterial cell membranes, 1,2-dioleoyl-sn-glycero-3-phosphoethanolamine (DOPE). They can be surface-patterned by microfluidic systems[32] or by a glass pipette connected to a micromanipulator.[34] We will take an advantage of its nanoscale size and study its potential as a starting material for pyrolysis.

Results

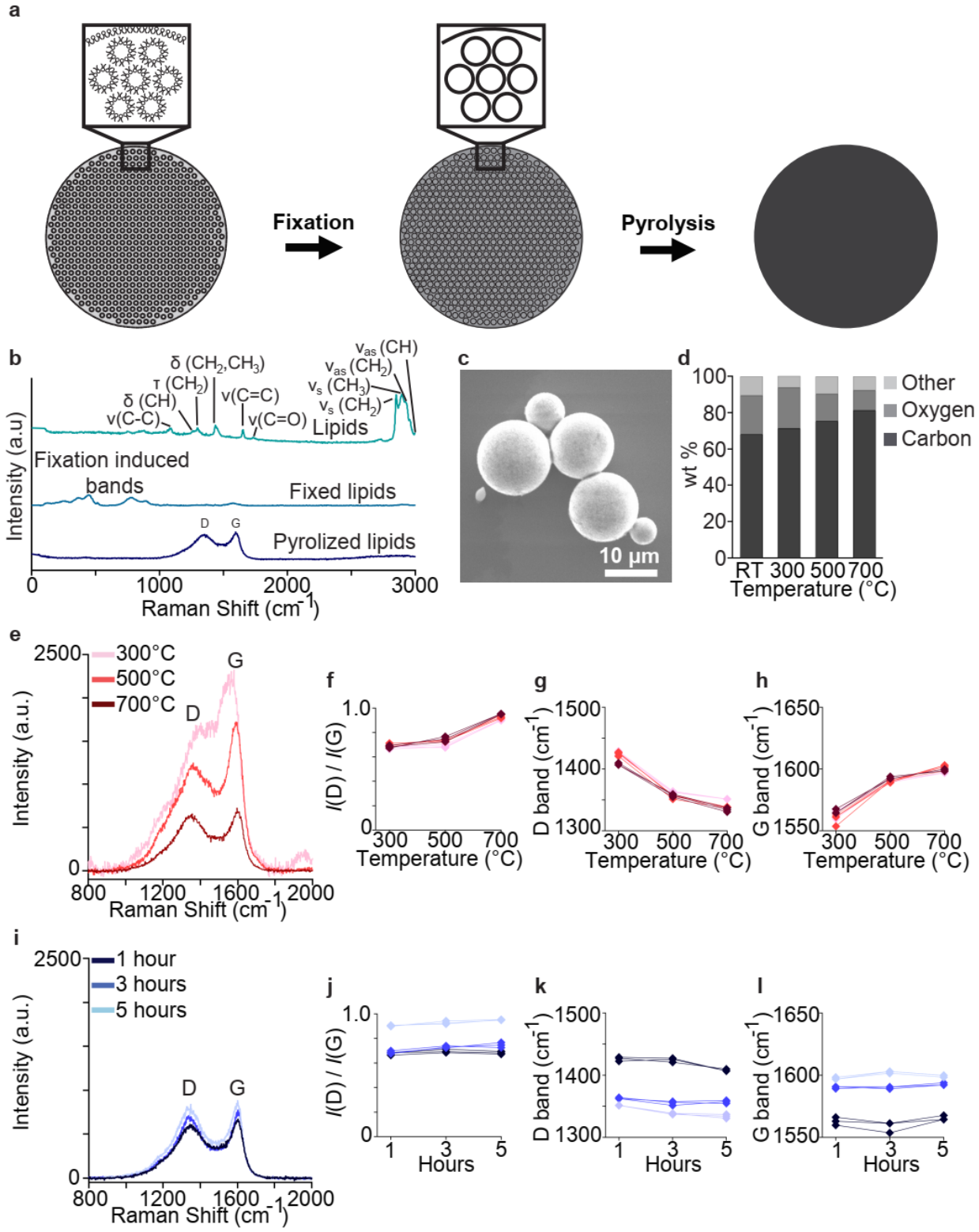
a
Fixation
Pyrolysis
b
δ (CH2,CH3)
τ (CH2)
δ (CH)
ν(C-C)
ν(C=C)
ν(C=O)
νas (CH)
νas (CH2)
νs (CH3)
νs (CH2)
Lipids
Fixation induced bands
Fixed lipids
D
G
Pyrolized lipids
Intensity (a.u)
Raman Shift (cm-1)
c
10 µm
d
Other
Oxygen
Carbon
wt %
RT 300 500 700
Temperature (°C)
e
300°C
500°C
700°C
D
G
Intensity (a.u.)
Raman Shift (cm-1)
f
I(D) / I(G)
Temperature (°C)
g
D band (cm-1)
Temperature (°C)
h
G band (cm-1)
Temperature (°C)
i
1 hour
3 hours
5 hours
D
G
Intensity (a.u.)
Raman Shift (cm-1)
j
I(D) / I(G)
Hours
k
D band (cm-1)
Hours
l
G band (cm-1)
Hours

Fig 1 Pyrolysis of lipid blocks. a Schematic illustration of lipid blocks in inverted hexagonal phase (H_{II}) before and after fixation and pyrolysis. **b** Raman spectra of lipids, fixed lipids and pyrolyzed lipids. **c** A scanning electron microscopy (SEM) image of lipid H_{II} blocks after fixation and pyrolysis. **d** A bar plot of wt% of elements in lipid blocks before and after pyrolysis at different temperature estimated by energy-dispersive X-ray spectroscopy (EDX). **e** Raman spectra of lipid blocks after pyrolysis for 1 h at 300 °C, 500 °C and 700 °C. Temperature dependence of (**f**) the intensity ratios between D and G bands and (**g**), (**h**) their positions. **i** Raman spectra of lipid blocks after pyrolysis at 700 °C for 1 h, 3 h and 5 hours. Time dependence of the (**j**) intensity ratios of D and G bands and (**k**), (**l**) their positions.

Raman spectroscopy and energy-dispersive X-ray spectroscopy (EDX) of H_{II} lipid blocks suggest that their fixation and pyrolysis yielded NC-graphite with 80% carbon content. To understand the pyrolysis process of DOPE lipids, first we characterize the samples made of DOPE lipid blocks in the inverted hexagonal (H_{II}) phase (Fig 1a) deposited on substrates, which are the reservoir for the protrusion of LNTs. We started with the characterization of these lipid blocks instead of LNTs because their high lipid density was compatible with standard Raman microscopy and energy-dispersive X-ray spectroscopy (EDX), whereas LNTs require more sophisticated tools (*e.g.* tip-enhanced Raman spectroscopy, TERS) for the detection of signals due to their low density on surfaces as we will present later. H_{II} lipid blocks were self-assembled by hydrating DOPE lipids with a HEPES buffer solution, followed by sonication (see Methods or ref[32] for details). These lipid blocks were chemically fixed with a combination of glutaraldehyde and osmium tetroxide, which are widely used in biology to prepare samples for electron microscopy.[37] Glutaraldehyde crosslinks lipid head groups, whereas osmium tetroxide reacts on the lipid tails, efficiently solidifying the entire lipid blocks.[35] Next these fixed lipid blocks are annealed under Ar atmosphere at 2×10^{-7} mbar at 300, 500 and 700°C for 1, 3, and 5 hours for pyrolysis. The evolution of Raman spectra from non-fixed lipid samples, after fixation, and after pyrolysis are shown in Fig 1b. The initial DOPE lipid shares common bands from oleic acid[38] (see Table S1) with the band at 2999 cm^{-1} assigned to the asymmetric stretching of CH, the bands at 2929 cm^{-1} and 2851 cm^{-1} assigned to the asymmetric stretching of CH_2, and the band at 2895 cm^{-1} assigned to the symmetric

stretching of CH_3. The bands at 1437 cm^{-1} and at 1298 cm^{-1} can be assigned to the bending of CH_2/CH_3 groups and the torsion of CH_2, respectively. The bands at 1733 cm^{-1}, 1654 cm^{-1}, and 1261 cm^{-1} can be assigned to the stretching of C=O and C=C, and the bending of CH, respectively. The band at 1084 cm^{-1} can be assigned to the stretching of C-C. The Raman spectrum for fixed lipids has almost none of these bands left, indicating that double bonds (*e.g.* C=O, C=C) are opened and used for the crosslinking reactions,[39-42] which made the entire structure solid to abolish all the vibrations such as CH, CH_2, CH_3, C-C stretching, CH_2/CH_3 bending and CH_2 torsion. Besides, a broad band appeared in the range of 130 – 900 cm^{-1}, which are osmium-related peaks such as stretching of Os-O although their separation is difficult. After the pyrolysis, these lipid blocks remained spherical as imaged by scanning electron microscopy (SEM, Fig 1c, Fig. S2), while in the Raman spectrum characteristic D and G bands from pyrolytic carbon appeared (Fig 1b). Elevating the pyrolysis temperature from 300°C to 700°C eliminated oxygen and increased the carbon content inside the samples as evidenced by Energy-dispersive X-ray spectroscopy (EDX) analysis (Fig 1d). A similar trend was previously observed during pyrolysis with SU-8 templates.[5]

The annealing temperature also affected the structure of the pyrolyzed carbon as Raman spectra reveal a temperature dependence (Fig 1e), whereas the effect of the annealing time was minimum (Fig 1i). First, the intensity of Raman spectra declined as the temperature increased (Fig 1e) probably because of the loss of materials from the substrate during pyrolysis. Two broad bands at approximately 1395 cm^{-1} and 1555 cm^{-1}, characteristic for the disorder-induced band (D-band) and the graphitic band (G-band), respectively, were observed after annealing. The I(D)/I(G) ratio enhanced as the pyrolysis temperature was elevated (Fig 1f). This may seem counterintuitive, because it looks as if pyrolysis is inducing the disorder (since the disorder-induced peak is increasing) instead of crystallizing the sample. Similar data were previously reported with

photoresist templates and were interpreted similarly.[2] However, the former extensive studies on the evolution of Raman spectra during the carbon crystallization process[43] suggests that this increase in I(D)/I(G) ratio actually indicates a crystallization process from amorphous carbon to nanocrystalline graphite. During the crystallization from amorphous carbon (a-C) over nanocrystalline graphite (NC-graphite) to a single crystal graphite, the I(D)/I(G) ratio does not change monotonically but first increases from a-C to NC-graphite, peaks at NC-graphite and decreases towards single crystal graphite. This is linked to the fact that the D band is associated with the breakage of symmetry occurring at the edges of graphite sheets, which first increases from a-C to NC-graphite because the initial amorphous carbon (a-C) lacks a graphite structure, thus does not even have D peak. Once graphite nanodomains start to form the D peak develops, yet at a certain point it decreases as these defects are eliminated towards single graphite crystal. Therefore, the interpretation of the I(D)/I(G) ratio requires an identification on which side of the slope we are. This can be performed by looking at the position of the G peak. In our data, the G peak shifted from 1560 cm^{-1} to 1600 cm^{-1} as temperature increased (Fig 1h), whereas the D peak decreased from 1445 cm^{-1} to 1350 cm^{-1}. This is consistent with the transition from a-C to NC-graphite.[43] Note that the small peak at around 1900 cm^{-1} for 300 °C in Fig 1e may come from C=C stretching formed during crosslinking, yet this vanishes at higher temperature annealing. Overall the results from lipid blocks suggest that their fixation and pyrolysis yielded NC-graphite with 80% carbon content.

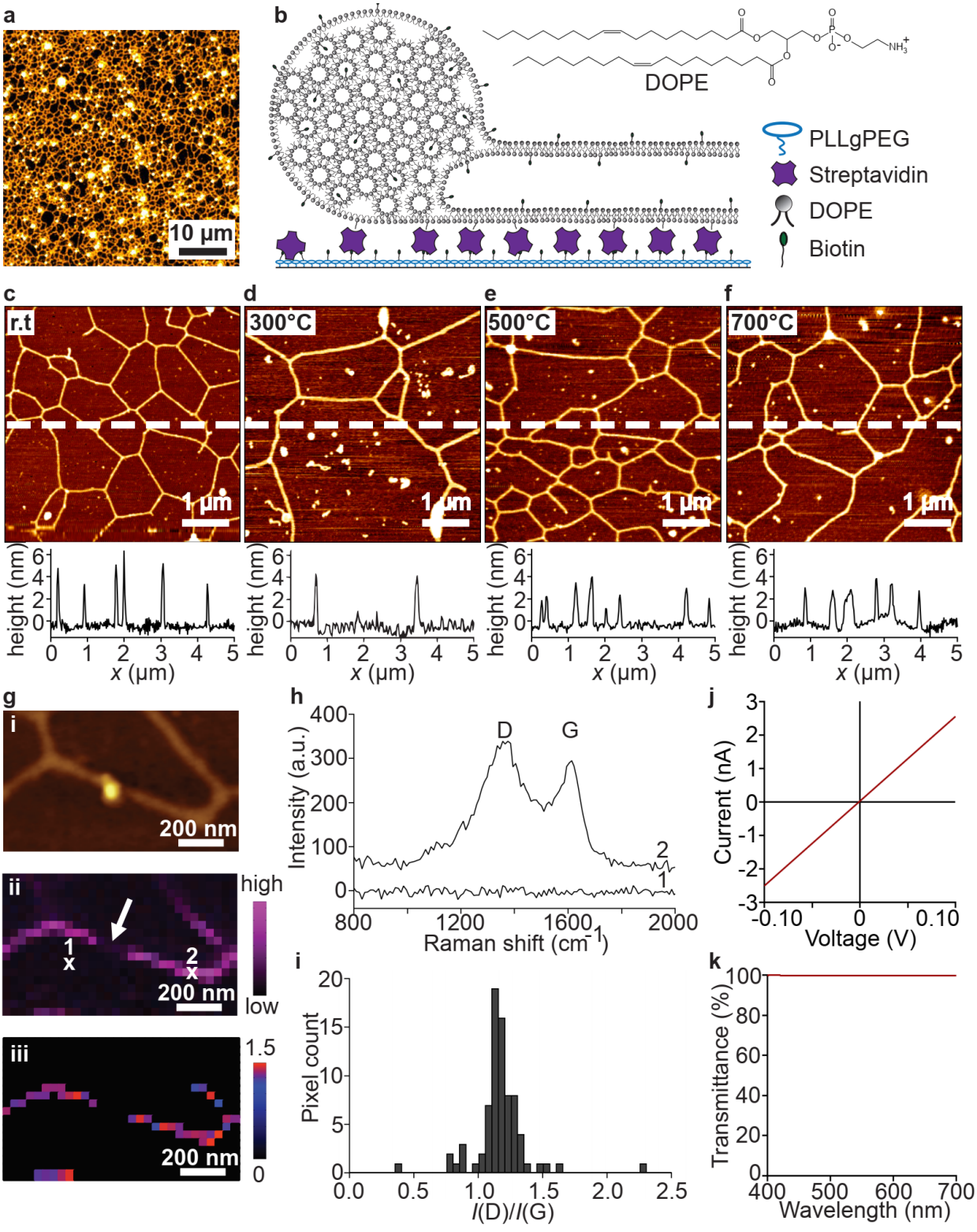

Fig. 2 Pyrolysis of LNTs assembled on substrates. a A fluorescent image of lipid nanotubes (LNTs). **b** A schematic illustration of the formation of LNTs from a lipid block on a functionalized substrate. AFM images and corresponding cross sections of LNTs (**c**) before and after pyrolysis at (**d**) 300 °C, (**e**) 500 °C and (**f**) 700 °C for 1 h on a silicon wafer. **gi** AFM topography of LNTs after pyrolysis, (**gii**) The integration of the intensity from D and G peaks from Tip-enhanced Raman spectroscopy (TERS) measured on

LNTs after pyrolysis, (**giii**) *I*(D)/*I*(G) ratio map. **h** Raman spectra at pixels indicated at 1 and 2 in (**gii**). **i** Histogram of *I*(D)/*I*(G) ratios from the pyrolysed LNT in (**g**). **j** *I*-*V* curve and (**k**) UV-VIS transmission of pyrolysed LNTs.

Fixation and pyrolysis of lipid nanotubes (LNTs) formed carbon nanoribbons with the width of 40 nm. Next, we applied the same fixing and pyrolysis process on LNTs assembled on substrates. These LNTs were protruded from DOPE blocks by applying sheer stresses (Fig. 2a, b), see Methods and reference[32]). LNTs consist of a single bilayer wall with a diameter of around 20 nm. Their chemical fixation flattens the tube structure into a ribbon as their AFM height shows around 5 nm (Fig. 2c). These LNTs withstand the pyrolysis up to 700°C (Fig. 2d-f), whereas they were evaporated at 800°C (Fig. S1).

To obtain their structural information, we characterized them by tip-enhanced Raman spectroscopy (TERS) as the standard Raman microscopy did not produce signals due to the low sample coverage on the substrates. Fig. 2gi is the topology of LNTs after pyrolysis at 700°C for 1 hours. The corresponding TERS intensity map (Fig. 2gii), which is a spatial mapping of the total intensity count from D- and G-bands (1150-1709 cm^{-1} for D and 1477-1722 cm^{-1} for G band, respectively), suggests a successful crystallization also in the case of LNTs. D and G peaks characteristic for NC-graphite were observed only on the ribbon structure, whereas no signal was detected on the background (Fig. 2gi-ii, h) This proves that the NC-graphite formed as a consequence of LNT pyrolysis. The histogram of the *I*(D)/*I*(G) ratio from these spectra shows that the average is around *I*(D)/*I*(G) = 1.2 (Fig. 2i), indicating a slightly higher degree of crystallization compared to the equivalent sample made of lipid blocks (Fig 1f). Its spatial map presents some spots with high *I*(D)/*I*(G) ratio shown in the red color in Fig. 2giii, suggesting the existence of highly crystalline domains. These carbon nanoribbons made by LNT pyrolysis are electrically conductive (Fig. 2j) and optically transparent (Fig. 2k). The conductivity of the carbon nanowires is roughly estimated

as 85 S/m, supposing that the dimension of a single carbon wire is 3 nm in height, 40 nm in width, and 2 mm in length, where 5000 wires are connected in parallel between gold contact pads (see Fig. S3 for the details). This is in the same order of magnitude as other pyrolytic carbon nanostructures[20] while several orders of magnitude lower than the value from a single graphene nanoribbon.[44,45] Generally, the conductivity of pyrolysed carbon is lower than for single carbon crystals due to unavoidable defects. Such a defect can be also seen in our TERS measurement (arrow in Fig. 2gii), where a lack of D and G peaks suggest that the carbon crystal is locally disconnected. The transparency of these samples was nearly the same as that of glass substrates. Considering the fact that even a graphene layer has 90% transparence, their extreme high transparency comes from the low carbon coverage of glass as it can be seen in the AFM image (Fig. 2c).

Conclusion

In conclusion, we demonstrated the fabrication of surface-attached carbon nanoribbons with 40 nm width by fixation and pyrolysis of LNTs. The fixation and pyrolysis conditions used in this work yielded NC-graphite with 80% carbon content, where the spatial mapping of I(D)/I(G) on the fabricated carbon ribbons indicated the existence of highly crystalline domains. These carbon nanoribbon-functionalized glass substrates are electrically conductive and optically as transparent as glass coverslips. Our approach takes advantages of the self-assembly of biomolecules to form organic nanostructure templates in contrast to the conventional method that uses photoresist combined with lithography. This approach based on biomolecular self-assembly is cheap, rapid, high-throughput, and enables a feature size of 40 nm by taking advantages of the nature-made

nanostructures. The demonstrated surface-patterned carbon nanowires may find applications towards conductive transparent substrates or nanowire biosensing in future.

Methods

Buffer solution (HEPES). Lipid nanotube (LNT) fabrication was performed in HEPES buffer solution at pH 7.4. The buffer solution was prepared with 0.15 M sodium chloride (Sigma-Aldrich, Switzerland) and 10 mM 4-(2-hydroxyethyl)piperazine-1-ethanesulfonic acid (HEPES, Sigma-Aldrich, Switzerland) in ultrapure water filtered through MilliQ Gradient A10 filters (Millipore AG, Switzerland). The pH was adjusted to 7.4 using 6 M NaOH (Sigma-Aldrich, Switzerland).

Surface functionalization with polyelectrolytes. PLL-g-PEG and PLL-g-PEG-biotin (Polylysine (20 kDa) grafted with polyethyleneglycol (2 kDa), #PLL(20)-g[3.5]-PEG(2)) were purchased from SuSoS AG (Switzerland) and dissolved in ultrapure water at 0.1 mg mL^{-1}. An oxygen-plasma-treated glass coverslip was incubated under PLL-g-PEG/PLL-g-PEG-biotin solution (2:1) for 30 min and rinsed with ultrapure water. The mixture of biotin-tagged PLL-g-PEG and PLL-g-PEG permits to control the density of biotin exposed on the surface. The same method was used for the coating of silicon wafers for scanning electron microscopy (SEM) that requires conductive substrates. After the functionalization of the surfaces, these substrates were incubated in streptavidin (#S4762, Sigma-Aldrich, Switzerland) solution (50 μg mL^{-1}) for 45 min and rinsed with ultrapure water.

Preparation of lipid self-assembled nanostructures. The lipids 1,2-dioleoyl-*sn*-glycero-3-phosphoethanolamine (DOPE, #850725), 1,2-dioleoyl-*sn*-glycero-3-phosphoethanolamine-N-(cap biotinyl) (BiotinPE, #870273), and 1,2-dioleoyl-*sn*-glycero-3-phosphoethanolamine-N-(lissaminerhodamine B sulfonyl) (RhodaminePE, #810150) were purchased from Avanti Polar Lipids and stored in chloroform. The lipid block solution was prepared by adding DOPE in a flask, drying in vacuum for minimum 2 h and adding HEPES buffer solution, followed by sonication at the final concentration of 1.0 mg mL^{-1}. Upon sonication, lipids detach from the flask wall and form blocks of the inverted hexagonal phase (H_{II}) phase. Experiments reported in Fig 1 were performed with these lipid blocks in solution in the sample chambers. The lipid nanotubes were prepared as reported in our previous work.[35] In this case, the lipid solution was prepared by mixing 96% DOPE + 4% BiotinPE + 0.1% RhodaminePE in a flask, drying in vacuum for minimum 2 h and adding HEPES buffer solution, followed by sonication at the final concentration of 1.0 mg mL^{-1}. Upon sonication, lipids detach from the flask wall and form blocks of H_{II} phase. The lipid blocks were adsorbed onto the substrates coated with PLL-g-PEG-biotin-streptavidin. The interaction between BiotinPE and the streptavidin exposed on the surface promotes the attachment of the lipids, while the PEG passivates the nonspecific adsorption. A turbulent flow was given by a pipette to create random LNT networks followed by rinse with HEPES buffer solution.

Sample chambers. All samples were confined in sample chambers consisting of a donut-shaped polydimethylsiloxane (PDMS) block and a glass coverslip cleaned by an oxygen-plasma cleaner (TePla IoN 3Mz oxygen plasma machine, PVA TePla, Germany) just before the experiments. The PDMS blocks adhere to the glass surface and act as a wall to confine liquid inside.

Chemical fixation of samples. Lipid blocks and lipid nanotubes were chemically fixed as previously described.[35] The samples were incubated with osmium tetroxide (1% in 0.1 M cacodylate buffer solution, pH 7.4) and glutaraldehyde (2.5% in 0.1 M cacodylate buffer solution, pH 7.4) at 2:1 ratio at 0 °C for 30 min followed by rinse with HEPES buffer for three times. Then, the buffer solution was exchanged with ethanol gradually (15%, 30%, 50%, 75%, 80%, 95%, 100%) and finally exchanged with acetone. After the removal of acetone, the sample was completely dehydrated.

Pyrolysis of lipid nanostructures. All samples were pyrolysed in a High Temperature Vacuum Furnace (Model 1100-3080-M1 from THERMAL TECHNOLOGIES), equipped with metallic heaters, thermal shields, and molybdenum sample holders. No refractory ceramic parts were present, thus providing a very low degassing and high vacuum at high temperature. The heating chamber was evacuated by a pumping station made of a first-stage dry rotary pump and a second-stage turbo pump. The vacuum level was kept at 2×10^{-7} mbar. The furnace was operated under Ar flow between 0.15 and 0.2 litres/min and air was evacuated at high temperature prior to each sample treatment. The heating rate was 600°/h for each temperature measurement. Temperatures between 300°C and 900°C were evaluated for different times for several samples.

Fluorescent microscopy. The fluorescent image was taken with Nikon Eclipse Ti-E (Nikon, JP) equipped with a DS-Qi1 camera (Nikon, JP), a metal-halide fluorescence lamp (Nikon, JP) with a long-distance objective lens 40x (CFI S Plan Fluor ELWD, Nikon) and a fluorescent filter TRITC

(543/593). The contrast and the brightness were adjusted and the image was presented with a false color for the figure.

Scanning electron microscopy. Samples were prepared on silicon wafers in a similar way as on glass substrates. Imaging was carried out with a JEOL JSM-7600F (JEOL, Switzerland) in secondary electron imaging mode at energy levels of 5.0 kV and 20.0 kV at various magnifications. The contrast was adjusted for the figures. The instrument was equipped with an EDX detector (model SDD X-MAX N80).

Atomic force microscopy. Images were scanned on a Nanowizard 3 BioAFM (JPK Instruments, Berlin, Germany) with Micromasch HQ:NSC15/Cr-Au cantilevers in non-contact mode (setpoint: ≈ 15 nN, scan rate: 1.0 Hz). The images were processed using JPK Data Processing software (JPK Instruments, Berlin, Germany).

Raman characterization. Raman spectra were recorded between 500 and 3000 cm^{-1} on a Horiba Labram HR evolution Raman spectrometer. The instrument was equipped with a Nitrogen cooled CCD camera as detector with a long-distance objective lens 100x with a spot size around 2 µm in diameter. Each measurement was recorded at 0.04mW power with a 532 nm Ar laser for 10 minutes.

Tip-enhanced Raman spectroscopy. The Raman active phonon modes of pyrolysed LNTs were investigated by tip enhanced Raman spectroscopy (TERS) using red (638 nm) laser for excitation. TERS experiments were performed in side-illumination/side-collection configuration (XploRa NanoRaman™ platform, HORIBA Scientific). The achieved lateral resolution for TERS is in the range of 8 nm as determined on a reference sample with a silver coated TERS tip (Omni™ TERS probes, HORIBA Scientific). The acquisition time for each spectrum was 20 s. There were two spectra collected at each pixel (patented SpecTop Mode), one in contact mode at close proximity to the sample surface for the collection of the near-field and far-field signal and the second at a distance for far-field signal only. By subtracting first from the second, the near-field signal could be extracted.

UV-VIS spectroscopy. Absorption spectra were obtained with V-670 (Jasco, USA). The samples deposited on glass coverslips were fixed with a hand-made sample holder.

Electrical measurements. A cyclic voltammetry program with a two electrode setup was used to obtain *I–V* curves with an Autolab Potentiostat (Metrohm AG, Switzerland) equipped with Nova 2.1 software. Gold was sputtered with a mask made of an aluminum foil to avoid photolithography on the fragile samples by JEOL JFC-1200 Fine Coater (JEOL, Switzerland) for fabricating contact pads (roughly 5 mm in width and 2 mm distance between electrodes), which were connected to the potentiostat via crocodile connection.

Data availability

The data that support the findings of this study are available from the corresponding author upon reasonable request.

References

(1) Schueller, O. J. A.; Brittain, S. T.; Marzolin, C.; Whitesides, G. M. *Chem Mater* **1997**, *9*, 1399.

(2) Kostecki, R.; Schnyder, B.; Alliata, D.; Song, X.; Kinoshita, K.; Kotz, R. *Thin Solid Films* **2001**, *396*, 36.

(3) Wang, C. L.; Jia, G. Y.; Taherabadi, L. H.; Madou, M. J. *J Microelectromech S* **2005**, *14*, 348.

(4) Lee, J. A.; Lee, S.; Lee, K. C.; Il Park, S.; Lee, S. S. *J Micromech Microeng* **2008**, *18*.

(5) Tang, Z. R.; Shi, T. L.; Gong, J. E.; Nie, L.; Liu, S. Y. *Thin Solid Films* **2010**, *518*, 2701.

(6) De Volder, M. F. L.; Vansweevelt, R.; Wagner, P.; Reynaerts, D.; Van Hoof, C.; Hart, A. J. *ACS nano* **2011**, *5*, 6593.

(7) Amato, L.; Keller, S. S.; Heiskanen, A.; Dimaki, M.; Emneus, J.; Boisen, A.; Tenje, M. *Microelectron Eng* **2012**, *98*, 483.

(8) Kurek, M.; Larsen, F. K.; Larsen, P. E.; Schmid, S.; Boisen, A.; Keller, S. S. *Sensors-Basel* **2016**, *16*.

(9) Bauer, J.; Schroer, A.; Schwaiger, R.; Kraft, O. *Nat Mater* **2016**, *15*, 438.

(10) Natu, R.; Islam, M.; Gilmore, J.; Martinez-Duarte, R. *J Anal Appl Pyrol* **2018**, *131*, 17.

(11) Zhang, X.; Vyatskikh, A.; Gao, H. J.; Greer, J. R.; Li, X. Y. *Proc. Natl. Acad. Sci. U. S. A.* **2019**, *116*, 6665.

(12) Penmatsa, V.; Kawarada, H.; Wang, C. *Journal of Micromechanics and Microengineering* **2012**, *22*, 045024.

(13) Yang, Z.-D.; Yang, X.-Y.; Liu, T.; Chang, Z.-W.; Yin, Y.-B.; Zhang, X.-B.; Yan, J.-M.; Jiang, Q. *Small* **2018**, *14*, 1800590.

(14) Yang, X.-Y.; Xu, J.-J.; Chang, Z.-W.; Bao, D.; Yin, Y.-B.; Liu, T.; Yan, J.-M.; Liu, D.-P.; Zhang, Y.; Zhang, X.-B. *Advanced Energy Materials* **2018**, *8*, 1702242.

(15) Xu, J.-J.; Xu, D.; Wang, Z.-L.; Wang, H.-G.; Zhang, L.-L.; Zhang, X.-B. *Angewandte Chemie International Edition* **2013**, *52*, 3887.

(16) Xu, J.-J.; Wang, Z.-L.; Xu, D.; Meng, F.-Z.; Zhang, X.-B. *Energy & Environmental Science* **2014**, *7*, 2213.

(17) Chang, Z.; Xu, J.; Zhang, X. *Advanced Energy Materials* **2017**, *7*, 1700875.

(18) Amato, L.; Heiskanen, A.; Hansen, R.; Gammelgaard, L.; Rindzevicius, T.; Tenje, M.; Emneus, J.; Keller, S. S. *Carbon* **2015**, *94*, 792.

(19) Hemanth, S.; Halder, A.; Caviglia, C.; Chi, Q. J.; Keller, S. S. *Biosensors-Basel* **2018**, *8*.

(20) Lim, Y.; Heo, J. I.; Madou, M.; Shin, H. *Nanoscale Research Letters* **2013**, *8*.

(21) Wang, S.; Hsia, B.; Carraro, C.; Maboudian, R. *J Mater Chem A* **2014**, *2*, 7997.

(22) Zakhurdaeva, A.; Dietrich, P. I.; Holscher, H.; Koos, C.; Korvink, J. G.; Sharma, S. *Micromachines-Basel* **2017**, *8*.

(23) Yin, C.; He, L.; Wang, Y. F.; Liu, Z. H.; Zhang, G. B.; Zhao, K. N.; Tang, C. J.; Yan, M. Y.; Han, Y. L.; Mai, L. Q. *Rsc Adv* **2016**, *6*, 43436.

(24) Vyatskikh, A.; Delalande, S.; Kudo, A.; Zhang, X.; Portela, C. M.; Greer, J. R. *Nat Commun* **2018**, *9*.

(25) Pham, T. A.; Kim, P.; Kwak, M.; Suh, K. Y.; Kim, D. P. *Chem Commun* **2007**, 4021.

(26) Amato, L.; Schulte, L.; Heiskanen, A.; Keller, S. S.; Ndoni, S.; Emneus, J. *Electroanalysis* **2015**, *27*, 1544.

(27) Seniutinas, G.; Weber, A.; Padeste, C.; Sakellari, I.; Farsari, M.; David, C. *Microelectron Eng* **2018**, *191*, 25.

(28) Sanborn, J.; Oglęcka, K.; Kraut, R. S.; Parikh, A. N. *Faraday Discussions* **2013**, *161*, 167.

(29) Adler-Abramovich, L.; Aronov, D.; Beker, P.; Yevnin, M.; Stempler, S.; Buzhansky, L.; Rosenman, G.; Gazit, E. *Nature Nanotechnology* **2009**, *4*, 849.

(30) Tabaei, S. R.; Gillissen, J. J. J.; Kim, M. C.; Ho, J. C. S.; Liedberg, B.; Parikh, A. N.; Cho, N.-J. *Langmuir* **2016**, *32*, 5445.
(31) Nakao, H.; Tokonami, S.; Yamamoto, Y.; Shiigi, H.; Takeda, Y. *Chem Commun* **2014**, *50*, 11887.
(32) Sugihara, K.; Chami, M.; Derenyi, I.; Voros, J.; Zambelli, T. *Acs Nano* **2012**, *6*, 6626.
(33) Sugihara, K.; Delai, M.; Mahnna, R.; Kusch, J.; Poulikakos, D.; Voros, J.; Zambelli, T.; Ferrari, A. *Integrative biology : quantitative biosciences from nano to macro* **2013**, *5*, 423.
(34) Sugihara, K.; Rustom, A.; Spatz, J. P. *Soft Matter* **2015**, *11*, 2029.
(35) Jajcevic, K.; Chami, M.; Sugihara, K. *Small* **2016**, *12*, 4830.
(36) Kozintsev, A.; Sugihara, K. *Rsc Adv* **2017**, *7*, 20700.
(37) Eltoum, I.; Fredenburgh, J.; Myers, R. B.; Grizzle, W. E. *Journal of Histotechnology* **2001**, *24*, 173.
(38) Czamara, K.; Majzner, K.; Pacia, M. Z.; Kochan, K.; Kaczor, A.; Baranska, M. *Journal of Raman Spectroscopy* **2015**, *46*, 4.
(39) Litman, R. B.; Barrnett, R. J. *Journal of Ultrastructure Research* **1972**, *38*, 63.
(40) Riemersma, J. C. *Biochimica et Biophysica Acta (BBA) - Lipids and Lipid Metabolism* **1968**, *152*, 718.
(41) Yamashita, S. 2018.
(42) Kiernan, J. A. *Microscopy Today* **2018**, *8*, 8.
(43) Ferrari, A. C.; Robertson, J. *Phys Rev B* **2000**, *61*, 14095.
(44) Kosynkin, D. V.; Lu, W.; Sinitskii, A.; Pera, G.; Sun, Z. Z.; Tour, J. M. *Acs Nano* **2011**, *5*, 968.
(45) Jiao, L. Y.; Zhang, L.; Wang, X. R.; Diankov, G.; Dai, H. J. *Nature* **2009**, *458*, 877.

Acknowledgments

The research leading to these results has partly received funding from Swiss National Foundation, the Swiss National Centre of Competence in Research (NCCR) Chemical Biology, Foundation Ernst et Lucie Schmidheiny and Leading House for the Middle East and North Africa (University of Applied Sciences and Arts Western Switzerland), from Shiseido Female Researcher Science Grant, UTEC-UTokyo FSI Research Grant Program, the FY 2020 University of Tokyo Excellent Young Researcher, the Female Faculty Startup Grant, IIS COVID-19 special funding, the special fund of Institute of Industrial Science (the University of Tokyo), Japan Society for the Promotion of Science (JP20K22324), Inoue Foundation for Science, Naito Foundation and Kanamori Foundation. We thank Bioimaging center at the University of Geneva for access to TEM and SEM instruments and chemicals for fixation of samples, Prof. Patrycja Paruch for use of SEM instrument, Prof. Dirk

Van der Marel for the use of furnace and Raman instrument and Prof. Thomas Bürgi group for the use of UV-VIS spectrophotometer.

Author contributions

K.S. conceived the project and oversaw all the research phases. K.S. and K.J. designed the project. K.J. prepared the samples for the LNT part. A-M.S. prepared the samples for the lipid blocks part. J.K performed the TERS measurements. Data collection and analysis were conducted by K.J and A-M.S. All the authors contributed to and commented on this paper.

Competing interests

The authors declare no competing interests.

Additional information

Supplementary information for Table S1 and Fig. S1-3 is available for this paper.

Correspondence and requests for materials should be addressed to K.S.